Effects of Upper-Level Shear on the Structure and Maintenance of Strong Quasi-Linear Mesoscale Convective Systems

MICHAEL C. CONIGLIO, DAVID J. STENSRUD, AND LOUIS J. WICKER

NOAA/National Severe Storms Laboratory, Norman, Oklahoma

(Manuscript received 27 January 2005, in final form 13 September 2005)

ABSTRACT

Recent observational studies have shown that strong midlatitude mesoscale convective systems (MCSs) tend to decay as they move into environments with less instability and smaller deep-layer vertical wind shear. These observed shear profiles that contain significant upper-level shear are often different from the shear profiles considered to be the most favorable for the maintenance of strong, long-lived convective systems in some past idealized simulations. Thus, to explore the role of upper-level shear in strong MCS environments, a set of two-dimensional (2D) simulations of density currents within a dry, statically neutral environment is used to quantify the dependence of lifting along an idealized cold pool on the upper-level shear. A set of three-dimensional (3D) simulations of MCSs is produced to gauge the effects of the upper-level shear in a more realistic framework.

Results from the 2D experiments show that the addition of upper-level shear to a wind profile with weak to moderate low-level shear increases the vertical displacement of parcels despite a decrease in the vertical velocity along the cold pool interface. Parcels that are elevated above the surface (1–2 km) overturn and are responsible for the deep lifting in the deep-shear environments, while the surface-based parcels typically are lifted through the cold pool region in a rearward-sloping path. This deep overturning helps to maintain the leading convection and greatly increases the size and total precipitation output of the convective systems in more complex 3D simulations, even in the presence of 3D structures. These results show that the shear profile throughout the entire troposphere must be considered to gain a more complete understanding of the structure and maintenance of strong midlatitude MCSs.

1. Introduction

Organized mesoscale convective systems (MCSs; Zipser 1982; Parker and Johnson 2000) are important to understand because of their propensity to produce severe weather and heavy rainfall. MCSs are observed in many climates across the globe during all times of the year (LeMone et al. 1998; Laing and Fritsch 2000; Burke and Schultz 2004). This study focuses on MCSs that occur frequently in the midlatitude regions of the United States during the spring and summer months, which are often associated with widespread severe windstorms and/or extremely heavy rainfall (Fritsch et el. 1986; Johns and Hirt 1987).

Furthermore, this study focuses on the class of MCSs that develop a quasi-linear or arced region of strong convection along its leading edge. Researchers have employed convection-resolving numerical models to understand the physical connection between the environmental vertical wind shear, usually the low-level shear, and the behavior of these types of MCSs (Thorpe et al. 1982; Rotunno et al. 1988; Weisman et al. 1988; Moncrieff and Liu 1999; Coniglio and Stensrud 2001; Weisman and Rotunno 2004). Much of this work emphasizes the importance of the low-level shear to counter the effects of the organized cold thunderstorm outflow (cold pool) (Rotunno et al. 1988; Weisman et al. 1988). Weisman and Rotunno (2004, hereafter WR04) suggest that surface-based shear distributed to depths greater than 5 km is detrimental to producing strong quasi-2D convective systems by sighting the lessened overall condensation, rainfall, and surface winds in their simulations. Furthermore, they affirm that the overall system-scale structure under these conditions show little sensitivity to changes in the upper-level shear, do not contain line segments or bow echoes along or just behind the leading edge of the cold pool,

Corresponding author address: Dr. Michael C. Coniglio, National Severe Storms Laboratory, 1313 Halley Circle, Norman, OK 73069.
E-mail: Michael.Coniglio@noaa.gov

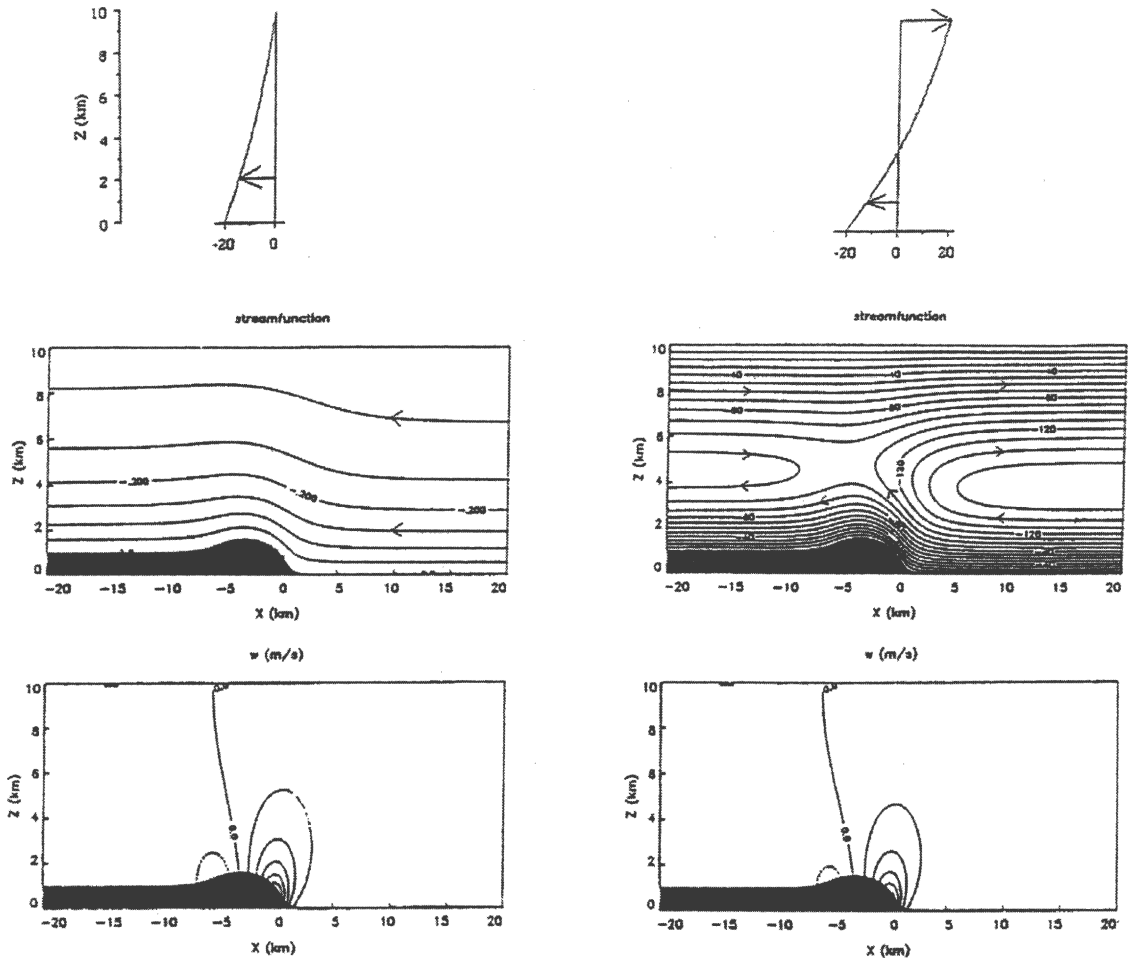

FIG. 1. Solutions adapted from the hydrodynamical model of S92. (top) Profiles representing changes in magnitude of the wind (m s^{-1}) with height in a reference frame fixed with the solid density current barrier (shaded in black in the middle panels). (middle) Values of the streamfunction and the direction of the flows and (bottom) vertical velocity (every 2 m s^{-1}).

and are not as strong or as organized as the systems that develop in zero upper-level shear.

This study is motivated by findings that relatively weak to moderate low-level shear and considerable upper-level shear is frequently observed in strong midlatitude MCS environments, including those that contain bow echoes and/or embedded supercells (Gale et al. 2002; Coniglio et al. 2004; Stensrud et al. 2005; Coniglio et al. 2005) and by the fact that the effects of these deep-shear environments are not emphasized in past 3D simulations.

Deep-shear environments and their effects on the lifting of environmental air above a cold pool have been examined in steady-state analytical frameworks based on conservation principles (Shapiro 1992; Xu 1992; Xu and Moncrieff 1994; Liu and Moncrieff 1996; Moncrieff and Liu 1999; Xue 2000; WR04). The results of Shapiro (1992, hereafter S92) are of particular interest to the present study. He uses an analytical 2D model of a fixed density-current barrier to hypothesize that an environment with larger deep-tropospheric shear decreases the vertical velocity of parcels along the barrier owing to less mass impinging on the barrier, but also increases the vertical displacement of parcels owing to longer residence times in the region of upward vertical motion. The flow that supports this behavior (see Fig. 1 for a schematic depiction) fits well within the idealized framework of 2D convection of Thorpe et al. (1982) summarized in Moncrieff (1992). Shapiro hypothesizes that these larger vertical displacements lead to a greater likelihood for initiating and maintaining convection, which is argued similarly in Moncrieff and Liu (1999) through the existence of a steering level (defined as the level at which the cold pool speed matches the environmental wind speed). However, the effects of the upper-level shear in S92 are not isolated since his model re-

quires an exponential decrease of shear with height (i.e., an increase in upper-level shear requires a greater increase in the low-level shear). A further limitation is that the density current is fixed as a barrier and thus cannot respond to the flow.

Similarly, a simple 2D vorticity–streamfunction model is presented in WR04 to explain the ability of a cold pool to lift environmental air. They show that for a given shear above a critical value the lifting of air is much greater when the shear is restricted to a depth that is 1/4 of the domain depth rather than when the shear is distributed over the full-domain depth. They use this to state that deep shear is fundamentally detrimental to the basic lifting of environmental air above a cold pool if the shear is distributed over a significant depth of the domain.

In addition to S92, the recent studies of Parker and Johnson (2004a,b,c, hereafter referred to as PJ04a,b,c, respectively, or, collectively, PJ04) are of particular interest to us as they present 2D and periodic 3D simulations of MCSs in deep shear. By focusing their attention on the 2D simulations, PJ04b and PJ04c analyze the dynamics of parcels as they pass through the convective region. They stress that the linear component of the perturbation pressure field generates downshear accelerations on the upshear sides of the updrafts in positive shear that largely account for the efficient overturning and the development of leading precipitation in deep shear environments. As in S92, they hypothesize that the shear gives air parcels more upright trajectories and allows them to spend more time in the zone of upward accelerations. Although most of their work focuses on the 2D results, we are intrigued that moderate 3–10 km shear allows for much more persistent updrafts in their periodic 3D simulations. Along with the observational evidence (Coniglio et al. 2004, hereafter C04; Burke and Schultz 2004; Coniglio et al. 2005), this suggests that physical mechanisms related to upper-level shear are relevant to both quasi-2D and 3D regimes of MCSs and suggests that it is important to continue the exploration of the effects of upper-level shear on the general characteristics of MCSs.

We first examine the ability of a cold pool to lift environmental air in a simplified model but take a somewhat different approach than S92 and WR04. We do not intend to compare different values of shear distributed over the full domain, as in S92, or full- versus quarter-domain-depth shear, as in WR04. Rather, our goal is to investigate how the behavior of the lifting is affected by the addition of shear above a profile that has a fixed magnitude of low-level shear. This is accomplished by producing a set of idealized 2D simulations of an evolving density current with the goal of quantifying the basic dependence of lifting on the upper-level shear. To build upon the results of PJ04, fully 3D simulations of convective systems are produced to show consistency of the 2D behavior to more realistic conditions and to detail the differences in structure with changes in the upper-level shear. We emphasize that the role of upper-level shear is particularly important to understand since the observed environments of strong midlatitude MCSs rarely have wind shear restricted to the lowest few kilometers (Stensrud et al. 2005).

The numerical modeling methods are outlined in section 2. Sections 3 and 4 describe the 2D and 3D numerical results, respectively. A summary of the main results and a brief discussion of the possible applications are found in section 5.

2. Methods

a. Configuration of the 2D simulations

The first exploration into the effects of upper-level shear is accomplished with idealized 2D simulations produced by the National Severe Storms Laboratory (NSSL) Collaborative Model for Multiscale Atmospheric Simulation (NCOMMAS) (see the appendix for a detailed description of the modeling system). A domain with horizontal (x) and vertical (z) dimensions of 240 and 16 km, respectively, is used with $\Delta x = \Delta z = 250$ m. As done in S92, the 2D simulations are initialized with a statically neutral thermal profile with the potential temperature (θ) set to 300 K to prevent buoyant convection. A heat sink of the form $A[\cos(\pi r/2)]^2$ is added to the θ tendency term to simulate a density current, where A is a constant controlling the maximum magnitude of the cooling and

$$r = \sqrt{\left[\frac{(x - x_c)}{x_r}\right]^2 + \left[\frac{(z - z_c)}{z_r}\right]^2}$$

controls the radius of influence of the cooling (the cooling is set to zero if $r > 1$). For all of the simulations, $A = -0.015$ K s^{-1}, $x_c = 120$ km, $z_c = 2$ km, $x_r = 10$ km, and $z_r = 2$ km. The parameter A is chosen iteratively such that the resultant surface θ perturbations (θ') in the vicinity of the density current leading edge are -6 to -8 K, which is well within the range of observed cold pools. The cooling is held constant throughout the duration of the simulations (1.5 h) in order to maintain a source of cold air for the leading portion of the density current to persist in a quasi-steady manner.

The initial ground-relative wind perpendicular to the

line approximates the median 0–0.5-, 0–1-, 0–2.5-, and 0–5-km shear[1] associated with strong MCSs (C04), but distributes this shear unidirectionally (Fig. 2). This wind profile from 0 to 5 km is held constant in all of the simulations. The effects of upper-level shear are examined in a set of seven simulations by varying the shear in the 5–10-km layer from 0 to 30 m s^{-1} in 5 m s^{-1} increments (Fig. 2).

b. Configuration of the 3D simulations

The same wind profiles that are used for the 2D simulations are used to produce a set of seven 3D simulations. In addition to liquid water processes, ice processes are represented with a three-class (ice, snow, graupel/hail) scheme (see Gilmore et al. 2004a). A constant Coriolis parameter is used with a value of 10^{-4} s^{-1}. Aside from these additional complexities, the current simulations are similar to the experiments presented in Weisman et al. (1988) and WR04, such that surface friction and radiation effects are ignored and a horizontally homogeneous initial condition is used to represent the environment.

A domain with cross-line (x) and along-line (y) lengths of 400 km and a height (z) of 16 km is used with $\Delta x = \Delta y = 2$ km. A constant Δz of 250 m is used below 1.25 km and is then stretched to about 700 m at the top of the model domain giving an average vertical spacing of about 500 m. Although Bryan et al. (2003) show that interpretations of MCS structure can be altered significantly with much higher resolution, these simulations are designed to be in the class of idealized simulations of Weisman (1993) and WR04, who used a grid with 1-km horizontal spacing.[2]

Using the C04 dataset, an initial temperature and moisture profile is derived from a set of 28 proximity soundings from strong MCS events valid at either 1800 or 0000 UTC in weakly forced situations to ensure a reasonable environment for MCS development (Fig. 3). The thermodynamic profile approximates the median values of convective available potential energy (CAPE), lifting condensation level (LCL), and the maximum vertical difference in equivalent potential temperature (θ_e) between low and midlevels found in the observational dataset (see Fig. 3 for these values). The most apparent differences in this sounding and the often-used idealized sounding that originated in Weisman and Klemp (1982) are the higher LCL and the drier conditions in midlevels.

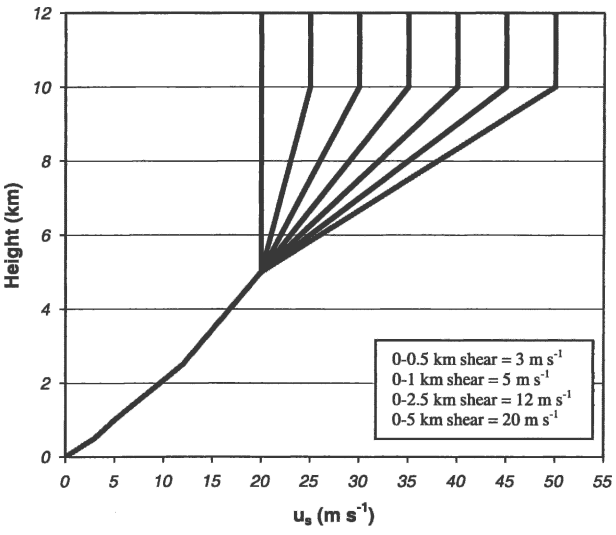

FIG. 2. Initial U profiles for the 2D and 3D simulations. The values of bulk shear in all profiles (listed on the figure) correspond to the median values derived from a set of weakly forced MCS proximity soundings (C04). The profiles that contain the values of shear closest to the median shear in the observations contains 20 m s^{-1} of shear from 0 to 5 km and 15 m s^{-1} of shear from 5 to 10 km.

A line of five θ' "bubbles" is used to initiate convection. Each bubble has a horizontal diameter of 10 km and a vertical diameter of 1.5 km. The line is oriented in the y direction and is centered at x = 200 km and y = 230 km. The initial θ' is 2 K at the center of the bubble and decreases to 0 K on the outer edge of the bubble. Random perturbations no greater than 0.25 K are added to each bubble to facilitate 3D structures. The model is then integrated for 6 hours to facilitate a comprehensive comparison to observations in terms of the maintenance and mature structure of MCSs.

3. Two-dimensional results

a. Density-current behavior

The most pertinent properties of the simulated density currents can be displayed through time-mean analyses for the period of 1.0–1.5 h for the 0, 10, and 20 m s^{-1} upper-level shear cases (Figs. 4–6) (hereafter, the cases with 0, 10, and 20 m s^{-1} of upper-level shear are referred to as 2D0, 2D10, and 2D20, respectively). The time-mean perturbation pressure field (p') shows well-known features of density currents, including a small region of positive p' ahead of the gust front (between x = 18 and x = 23 km in the bottom panel of Fig. 4), a

[1] For simplicity, the shear is approximated by the magnitude of the difference vector between the wind vectors at two different vertical levels.

[2] Weisman et al. (1997) show little difference in the convective structure and mean vertical flux characteristics for idealized simulations that use a horizontal grid resolution in the 1–2 km range.

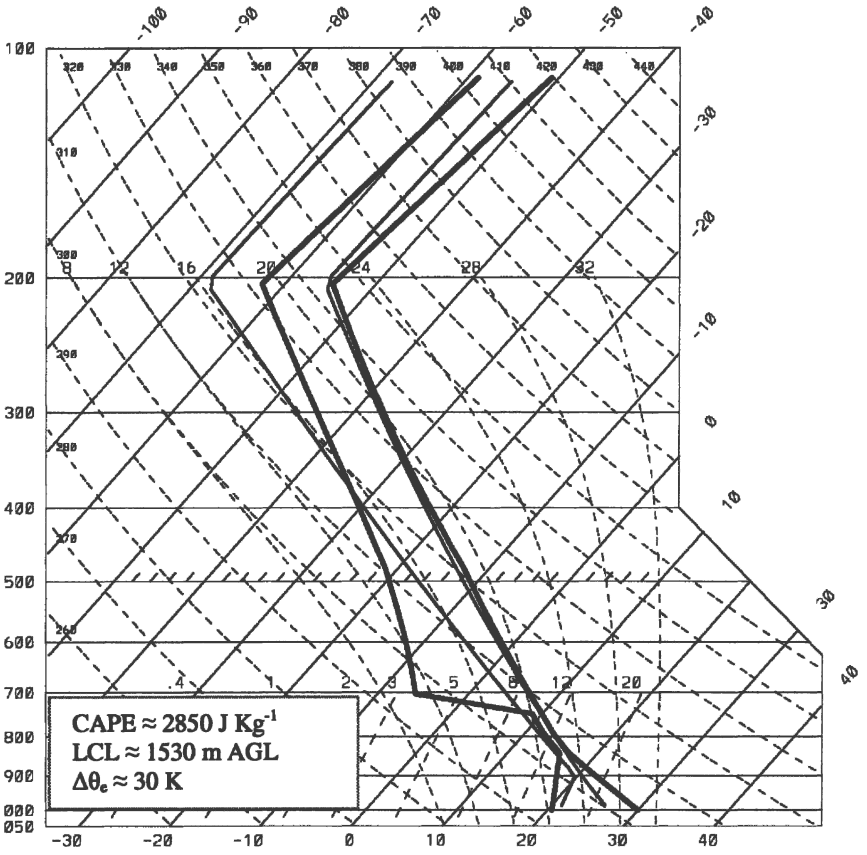

FIG. 3. Initial sounding used in the 3D simulations (thick lines) compared to the Weisman and Klemp (1982) sounding (thin lines). The values of CAPE, LCL, and the maximum difference in θ_e between low and midlevels ($\Delta\theta_e$) in the profiles (listed on the figure) correspond approximately to the median values derived from a set of weakly forced strong MCS proximity soundings.

broad region of positive p' induced by negative buoyancy near the surface (at $x < 18$ km and $z < 2$ km), and negative p' toward the rear of the cold pool head generated by the rotation associated with a large eddy vortex at the interface between the cold pool and the atmosphere above (generally in the area enclosed by $x = 4$ and $x = 16$ km and $z = 2$ and $z = 7$ km; Droegemeier and Wilhelmson 1987).

The density current head region, which is best identified by the region enclosed by the $\theta' = -0.5$ K contour in the top panels of Figs. 4–6 (this is used to define the head depth h), does not become as deep and does not expand as far rearward with time for 2D10 as compared to 2D0 (cf. Figs. 5 and 6). The p' field for 2D10 (Fig. 5, bottom panel) displays the same features as found for 2D0 and an additional region of positive p' above the head region related to a flow stagnation point (S92) (this is discussed in more detail in section 3b). For 2D20, the region of positive p' in upper levels becomes more pronounced (Fig. 6, bottom panel) and h is reduced further. In conjunction with these changes, the upward vertical velocity (w) decreases for the larger upper-level shears (Fig. 7) owing to the shallower currents and the weaker vertical pressure gradients along the interface. The speed of the downshear edge of the density current is generally 18–21 m s^{-1} among the simulations with 0–15 m s^{-1} of upper-level shear. The decrease in h, the weakening of w, and the contraction of the $\pm w$ couplet continues as the upper-level shear is increased to 30 m s^{-1} (not shown). The speed is reduced by 3–4 m s^{-1} in the stronger shear cases as a result of a shallower density current head (Seitter 1986).

These results show that an increase in shear above h results in a decrease in w along the interface and that the linear results from S92 would seem to be valid even for an evolving density current. This provides the possibility of testing the hypotheses of S92 that vertical parcel displacements can still be increased despite a reduction in w, which is investigated next.

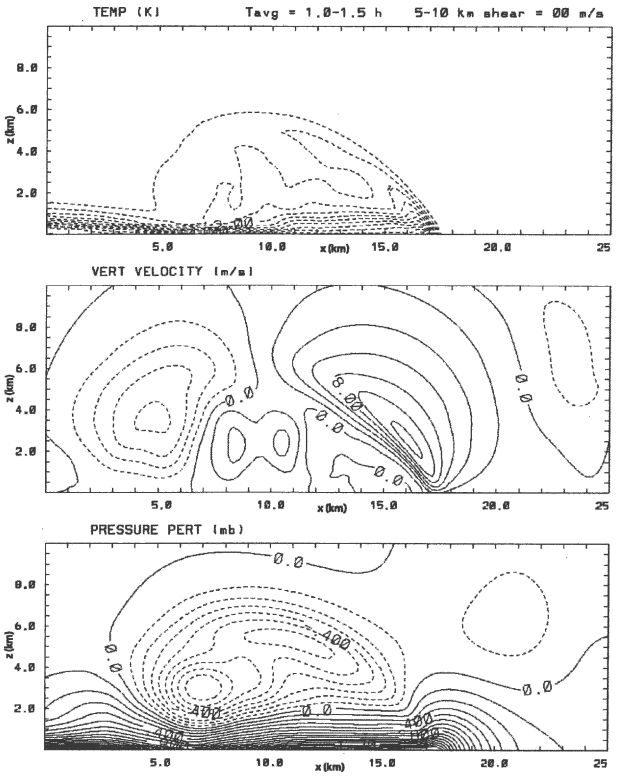

FIG. 4. Time-mean (1.0–1.5 h) values of perturbation potential temperature (contours every 0.5 K starting at −0.5 K), upward vertical motion (contours every 2 m s^{-1}), and perturbation pressure (contours every 0.1 h Pa with negative contours dashed) for 2D0. Only an $x = 25$ km by $z = 10$ km portion of the domain is shown with the gust front centered at $x = 17.5$ km.

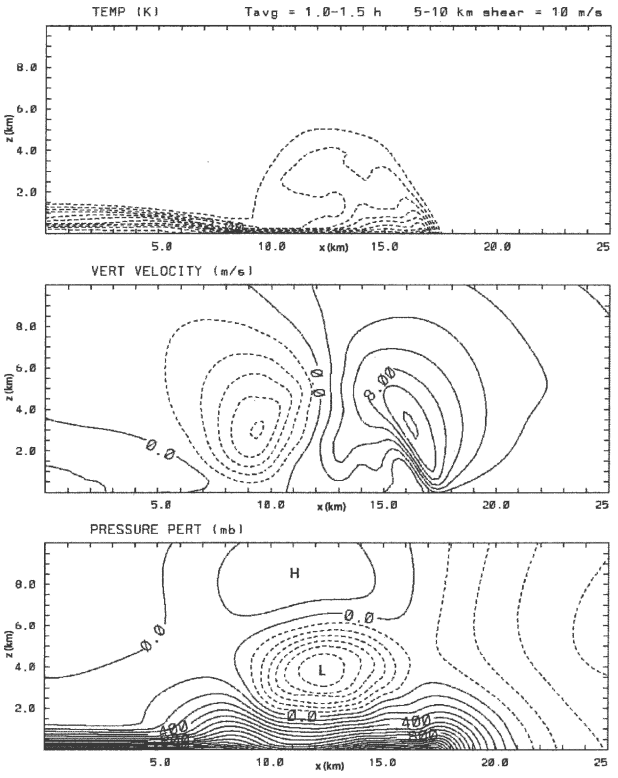

FIG. 5. As in Fig. 4 but for 2D10 with regions of relative high (H) and low (L) pressure noted.

b. Parcel analyses

Since the artificial cooling is introduced at a much shallower depth than the balanced, steady-state depths for conservative, bounded density currents (Xue et al. 1997), transience occurs to various degrees for most of the simulations. But the trade-off of this design is that h matches what is found in observations more than the idealized steady-state configurations in which h can extend to as much as three-quarters of the domain depth (Xue 2000). The occurrence of transience leads us to calculate the vertical displacements numerically using trajectories rather than using the streamfunction for the time-averaged flow. The trajectories are calculated based on the iterative methods outlined in Staniforth and Côté (1991) and are used to quantify the lifting of air among the set of 2D simulations. Trajectories are made from starting positions in the undisturbed flow ahead of the gust front at each model vertical level (every 250 m) between $z = 125$ m and $z = 1875$ m. The trajectories at each starting height are calculated using model output every 30 s and are calculated at starting times that vary from 1800 to 2400 s in 30-s increments, giving a total of 21 trajectories for each of the eight vertical starting positions for each simulation.

Despite the decrease in w associated with increases in upper-level shear (Fig. 7), the maximum vertical parcel displacements (δ_{max}) are actually larger for 2D5, 2D10, and 2D15 than they are for 2D0 (Fig. 8). Maximum displacements are about 7 km for zero upper-level shear and increase to a maximum of 9–11 km somewhere between 5 and 10 m s^{-1} of upper-level shear before decreasing to about 4 km for 30 m s^{-1} of upper-level shear (Fig. 7). Interpolation of the displacements suggests that they are roughly the same for 17 m s^{-1} of upper-level shear as they are for zero upper-level shear.

Further insight into this behavior is gained through an illustration of the trajectory paths for 2D0, 2D10, and 2D20 (Fig. 9). For 2D0, all of the parcels are lifted and quickly swept rearward along the density current interface (Fig. 9a). For 2D10, the parcels that begin below 1 km are forced over the density current and are swept rearward as before, but to slightly lower levels than for 2D0 owing to a slightly smaller head. However, the parcels that begin between $z = 1375$ m and $z = 1875$ m are found to be part of an overturning branch of the inflow (Fig. 9b). The flow then represents a mixture of

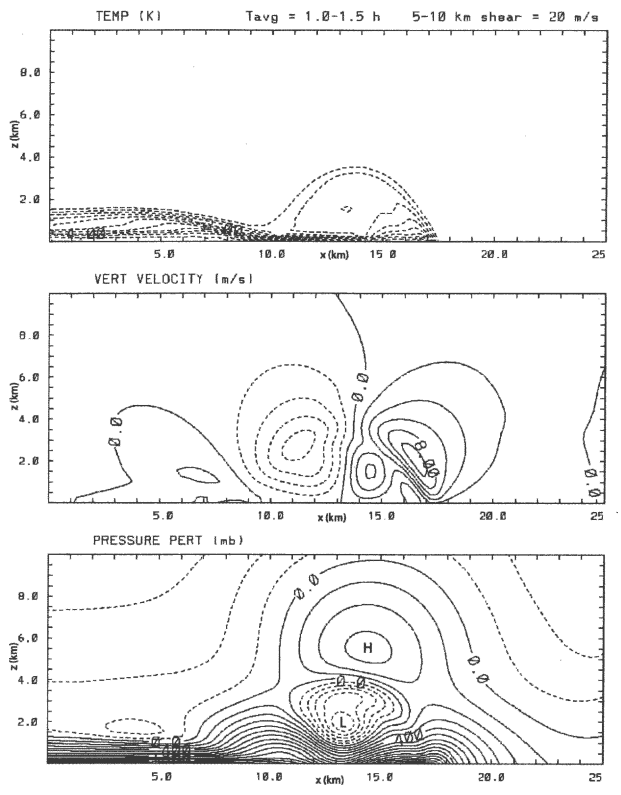

FIG. 6. As in Fig. 5 but for 2D20 with regions of relative high (H) and low (L) pressure noted.

rearward flowing and overturning airstreams that has long been identified in idealized frameworks of squall lines (Moncrieff 1992; S92; PJ04b). Inspection of the parcel paths reveals the most pertinent point that the parcels responsible for the deeper lifting for weak to moderate upper-level shear (Fig. 8) are found in the overturning updrafts. This overturning arises with the addition of upper-level shear to the low-level shear profile, which emphasizes the importance of the deeper shear in these situations.

The enhancement in 2D lifting provided by the upper-level shear does not continue for the stronger shears, however, as the distribution of δ_{max} shows that the lifting begins to decrease as the upper-level shear is increased beyond $\sim$10 m s^{-1} (Fig. 9). In these cases, the overturning is shallower but a stagnation point remains above the density current head region. As discussed in S92 and Xue et al. (1997), the region of relative high pressure aloft (Figs. 5 and 6, bottom panels) is a direct dynamical response to this flow stagnation. The density current circulation becomes shallower (Figs. 5 and 6) in the stronger shear regimes in response to the enhanced downward vertical pressure gradient force caused by the higher pressure aloft. Thus the elevated parcels moving front to rear are accelerated upward at a reduced rate in the stronger upper-level shear environments, which translates into shallower overturning (Fig. 9c). It is important to note, however, that the detrimental effects of the stronger upper-level shears on the 2D lifting of air do not apply directly to the 3D results, as shown later. This is because the removal of the 2D restriction allows for 3D convective structures to develop, which are particularly prevalent in the stronger deep shear as shown in Weisman et al. (1988), WR04, and later in this paper.

Finally, it is important to note that the upward branch of the overturning remains close to the leading edge of the density current. This raises the point about the importance of the steering level in the flow as similarly discussed in Moncrieff and Liu (1999). Whereas the underlying dynamics can be explained through the pressure perturbations that accelerate the inflowing parcels in the downshear direction, as explained in PJ04b, we argue that the steering level is important in the sense that it facilitates the horizontal placement of the upward branch of the overturning flow close to the leading edge of the cold pool. The presence of an updraft in positive shear will lead to downshear accelerations (PJ04) regardless of the presence of a steering level, but the lack of a steering level initially suggests that all cells will be inclined to maintain rearward velocities and convect at a farther distance behind the leading edge of the cold pool, despite the downshear accelerations. It will be shown later in the 3D results that this is a scenario that hinders the maintenance of the leading convection of MCSs. It is important to point out that the typical cold pool speeds observed with strong quasi-linear MCSs (15–25 m s^{-1}) and the typical deep-shear magnitudes observed with strong, quasi-linear MCSs (20–40 m s^{-1}) often facilitates steering levels in mid and upper levels during the initial stages of the MCSs (see C04), which implies that the downshear accelerations induced by mid- and upper-level shear (PJ04) will translate into overturning updrafts with cells closer to the gust front in most cases.

The preceding discussion builds on the analyses of S92 and PJ04b by quantifying the benefit of the 2D lifting in deep shear environments. In a sense, we have bridged the 2D work of S92 and PJ04 by considering an evolving cold pool but in a statically neutral environment (S92 only considers flow over a solid fixed obstacle without the possibility of buoyant convection and PJ04 consider both forced accelerations above an evolving cold pool and the feedbacks tied to buoyant convection). While we have confirmed the basic hypotheses of S92 and PJ04 that deeper lifting can be obtained in deeper shear environments, we have added

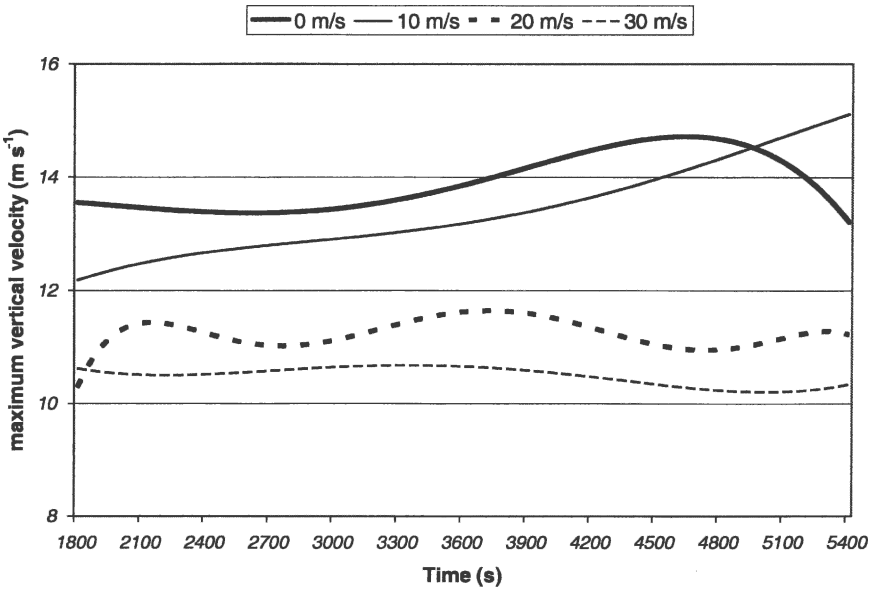

FIG. 7. Evolution of the maximum vertical velocity along the density current interface for the simulations with 0, 10, 20, and 30 m s^{-1} of upper-level shear.

that the introduction of shear entirely above an evolving cold pool can be beneficial to the lifting through overturning updrafts even in the absence of the downshear accelerations that result from the interactions between the shear and buoyant convection, which is the process described in PJ04. For the dimensions used in these experiments, the shear is added above 5 km, which generally marks the vertical extent of the density current head regions among the seven simulations. But we believe these results can be generalized to the addition of vertical shear layers that begin near the top of the cold pool regardless of the cold pool depth. The following section examines the effects of this enhanced lifting resulting from the addition of upper-level shear in more complex 3D simulations.

4. Three-dimensional results

Although seven simulations have been produced and analyzed, most of the important differences in system structure and evolution are presented sufficiently through a comparison of the simulations with 0, 15, and 30 m s^{-1} of shear from 5 to 10 km (hereafter, these simulations will be referred to as 3D0, 3D15, and 3D30, respectively).

a. Overview

The most significant differences among the simulations are found in the maximum and minimum values of vertical velocity after 2 h (Fig. 10), which coincides with the transition of a line of isolated convective cells into an organized MCS structure in all of the simulations. The updrafts and downdrafts for 3D0 weaken after this time, which marks the firm establishment of the cold pool (Fig. 11) and the beginning of an upshear-tilted phase. This trend continues for 3D0 until an equilibrium state is met at ~4 h (Figs. 10 and 11). In contrast, the maximum updrafts for 3D15 and 3D30 maintain

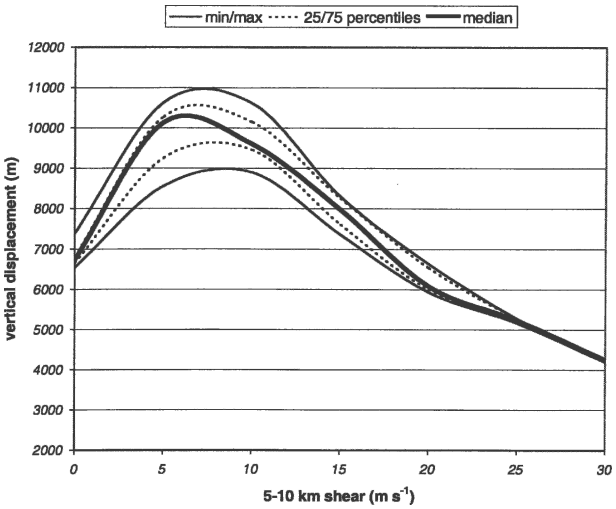

FIG. 8. Distribution of the maximum displacement (m) for any parcels in the lowest 2 km for various values of 5–10 km shear. Thin solid lines enclose the maximum and minimum values among the set of trajectory calculations described in section 3, thin dashed lines enclose the 25th and 75th percentiles, and the thick solid line is the median.

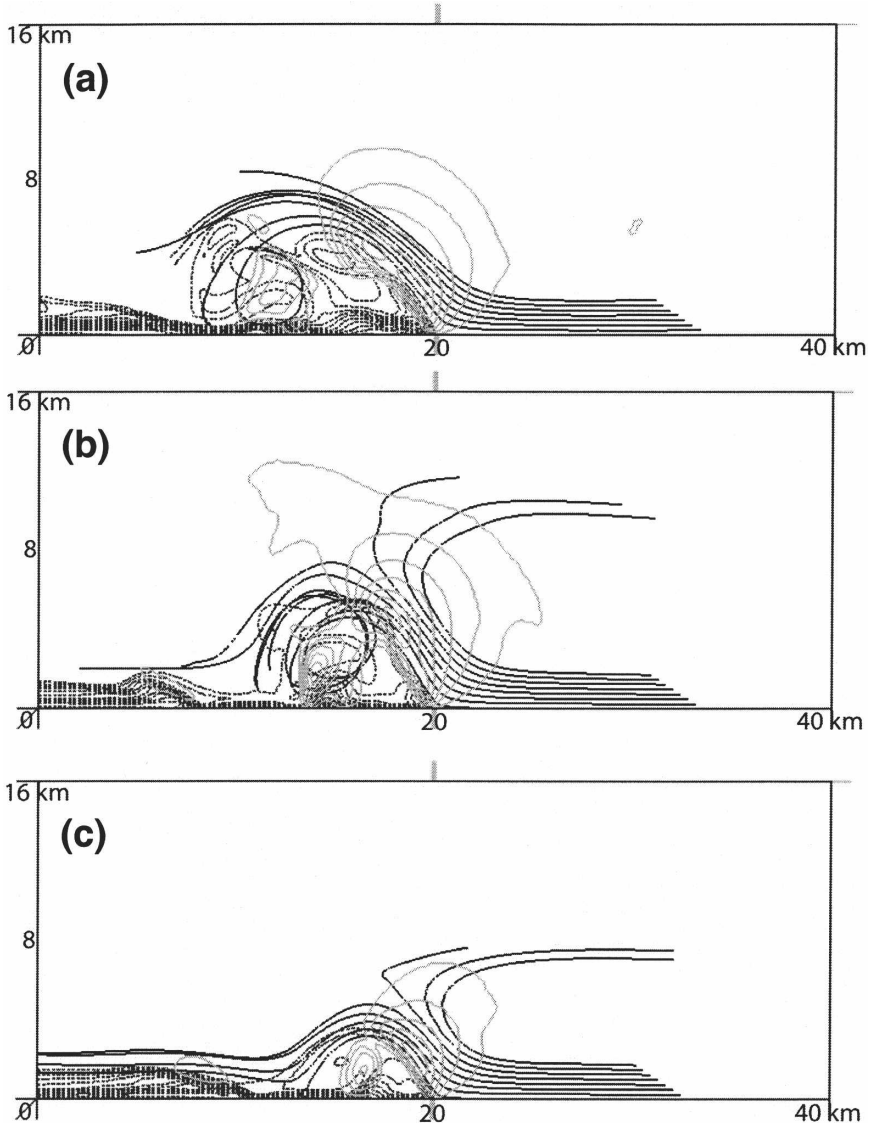

FIG. 9. Illustration of parcel paths in the lowest 2 km starting at 2100 s (thick black lines) for the (a) 0, (b) 10, and (c) 20 m s^{-1} shear cases. The parcel paths end at (a) 4200, (b) 4500, and (c) 5400 s. The perturbation potential temperature (thin dashed lines, contoured as in Fig. 4) and positive vertical velocity (thick gray lines, contoured every 2 m s^{-1} starting at 2 m s^{-1}) also are shown at these times.

their strength throughout the 6-h simulation time (Fig. 10a). As similarly found by WR04 and shown later in this paper, isolated supercell-like structures develop along the outer flanks of the system and produce strong updrafts. However, the updrafts along the center portion of the system for the simulations with upper-level shear are nonsupercellular through 6 h and are significantly stronger than the updrafts found for 3D0. These two factors, along with the maintenance of the precipitation intensity as shown later, contribute to a substantial increase the total precipitation output with the addition of upper-level shear (Fig. 12).

As an aside, we found that the evolution of the maximum surface wind speed is much less sensitive to changes in the upper-level shear than the vertical velocity (not shown). However, we have also found that it is difficult to generalize these results because sensitivity tests reveal that the strength of the surface winds and their aerial coverage are quite sensitive to changes in the experimental design, especially to parameters in the ice microphysics scheme. Understanding these sensitivities is beyond the scope of this paper but is paramount to understanding how the upper-level shear generally affects the surface winds associated with strong

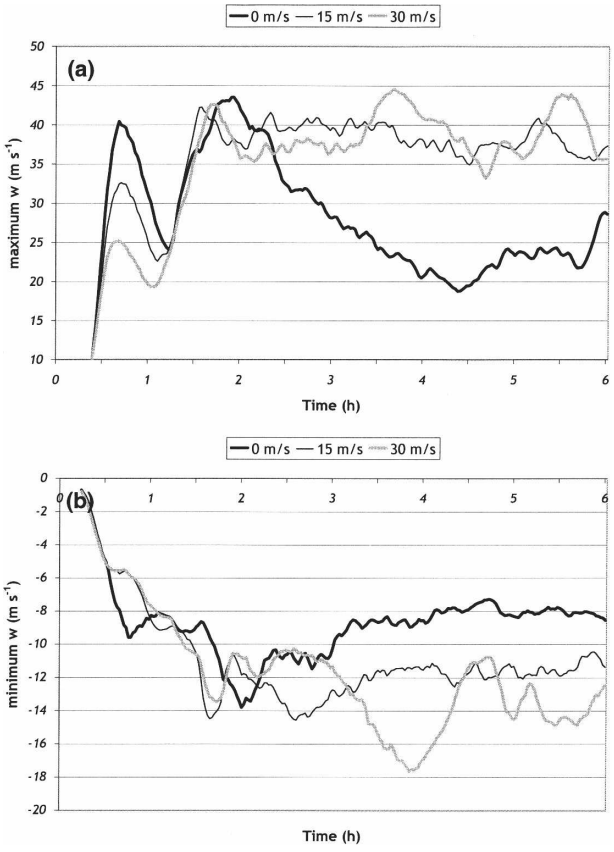

FIG. 10. Evolution of the (a) maximum and (b) minimum vertical velocity for 3D0, 3D15, and 3D30.

MCSs. However, the general evolution of the size and structure of the MCSs, and the tendency for the updrafts to be maintained for longer periods in environments with upper-level shear, is not as sensitive to these changes in the microphysics and provides greater confidence that the behavior of the simulations presented next is robust.

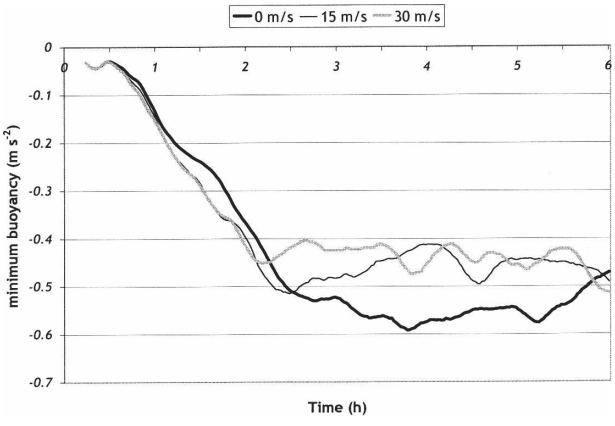

FIG. 11. Evolution of the minimum buoyancy acceleration for 3D0, 3D15, and 3D30.

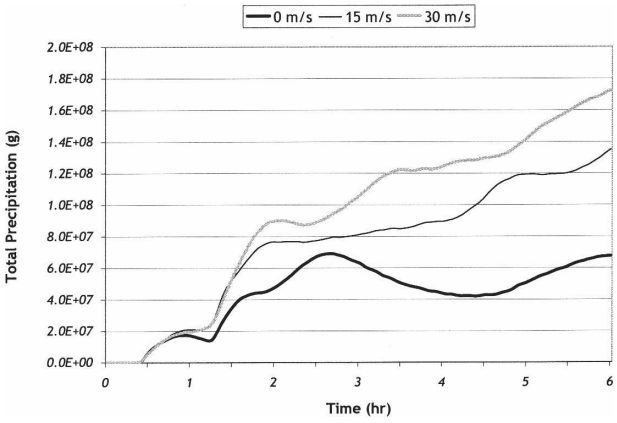

FIG. 12. Evolution of the domain-integrated rainwater for 3D0, 3D15, and 3D30.

b. *Differences in MCS structures*

The system for 3D0 begins as a line of convective cells located 10–30 km behind the surface gust front that evolves into an arc of convection about 100 km in length at 3 h (Fig. 13a). At later times, the cells are found farther behind the gust front (Figs. 13b–d). Organized rear inflow develops by 4 h, much of which descends to the surface at later times and is coincident with the weakening of the convective updrafts. This evolution is consistent with the well-known archetypal MCS with trailing stratiform precipitation (Houze et al. 1989) and with the simulations presented in Weisman and Trapp (2003) and WR04 that include moderate low-level shear and no upper-level shear.

The system for 3D15 begins similarly to the system for 3D0, then evolves into an arc of convection about 150 km in length located 10–15 km behind the gust front at 3 h (Fig. 14a). More isolated cells and supercell-like structures are found on the ends of the line, especially on the southern end. A cyclonic vortex with rear inflow becomes evident behind a more solid line of leading convection along the center of the cold pool, as for 3D0 but on a smaller scale. This structure produces a smaller area of trailing stratiform precipitation and the development of a small leading anvil of hydrometeors (approaching the front-fed leading stratiform structure that is simulated by PJ04 (not shown). The smaller-scale rear inflow contributes to the development of a well-defined bow echo along the center portion of the line for 3D15 (Fig. 14b). In the southern portion of the line, another bow echo feature develops from an individual cell at 3 h and surges to the south and east between 4 and 5 h (Figs. 14b and 14c). Rear inflow on a

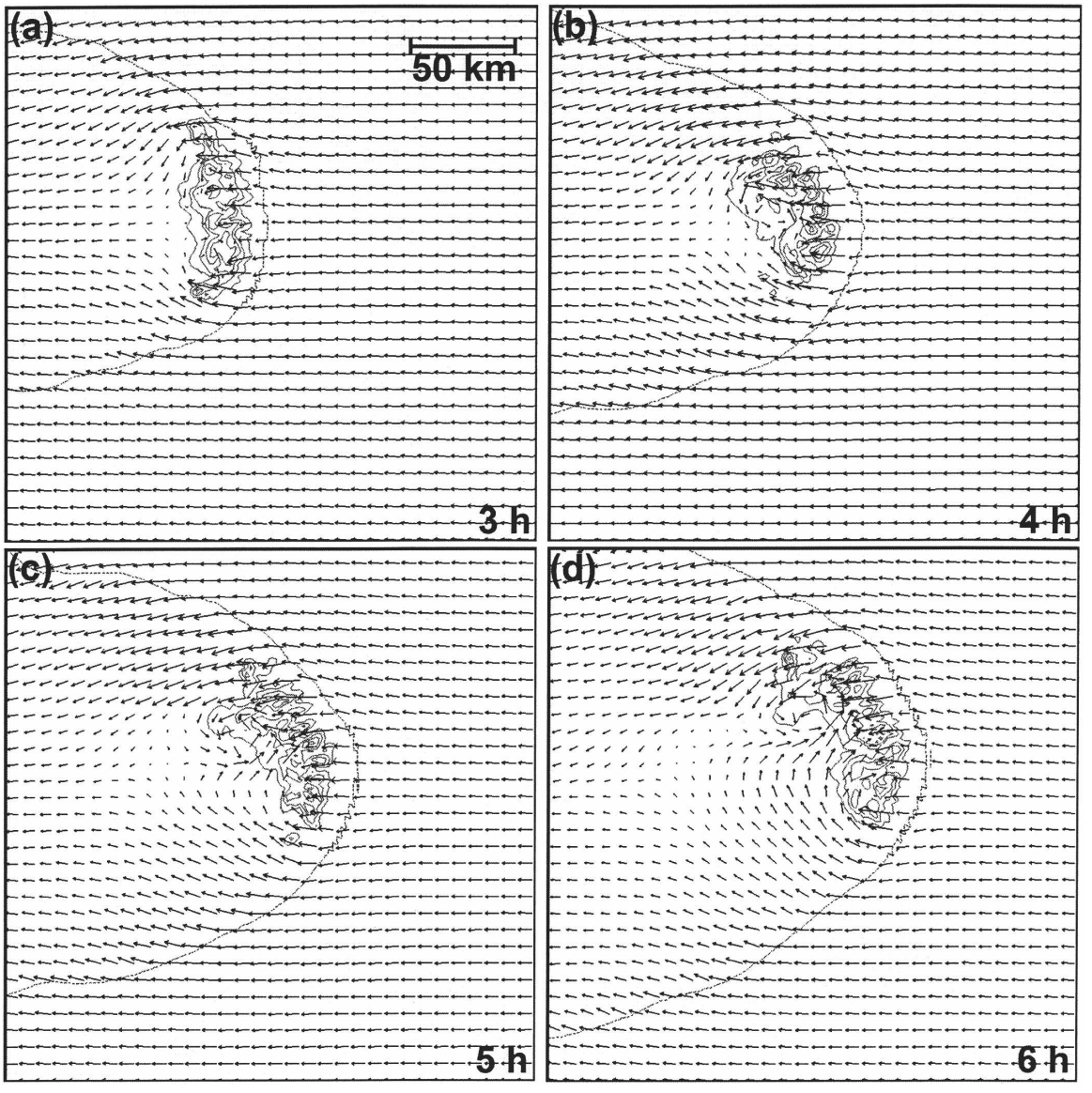

FIG. 13. A 240 km × 240 km portion of the domain with the total precipitation mixing ratio at 4 km AGL (solid lines contoured every 2 g kg^{-1} starting at 1 g kg^{-1}), the position of the gust front at the surface (dashed line), and the gust-front-relative wind at 3 km AGL at (a) 3, (b) 4, (c) 5, and (d) 6 h for 3D0. The winds are shown every four grid points (a vector length that covers four grid points corresponds to a wind magnitude of 10 m s^{-1}).

smaller scale compared to 3D0 continues into a line segment along the center and northern portions of the gust front at 6 h for 3D15 (Fig. 14d). Also notice that the line of leading convection for 3D15 (and for 3D30) is over twice as long as it is for 3D0 by 5 h, with a horizontal length scale of 250–300 km (cf. Figs. 13c and 14c). This contributes to the large increases in the total precipitation output of the systems as the upper-level shear is increased (Fig. 12) despite the fact that the cells are isolated along the ends of the line.

The structure for 3D30 is similar to 3D15 in terms of its size and the location of the cells behind the gust front (Fig. 15). Consistent with past simulations in very strong deep layer shear (Weisman et al. 1988; WR04), the individual convective cells retain their identity for longer periods than for shallower shears. However, a portion of the line toward the southern half of the system contains a solid line of convective cells that accelerates to the south and east ahead of a region of rear inflow. The highly 3D structure of the system is apparent in the significant northerly component to this rear inflow, which is most apparent at 6 h (Fig. 15d).

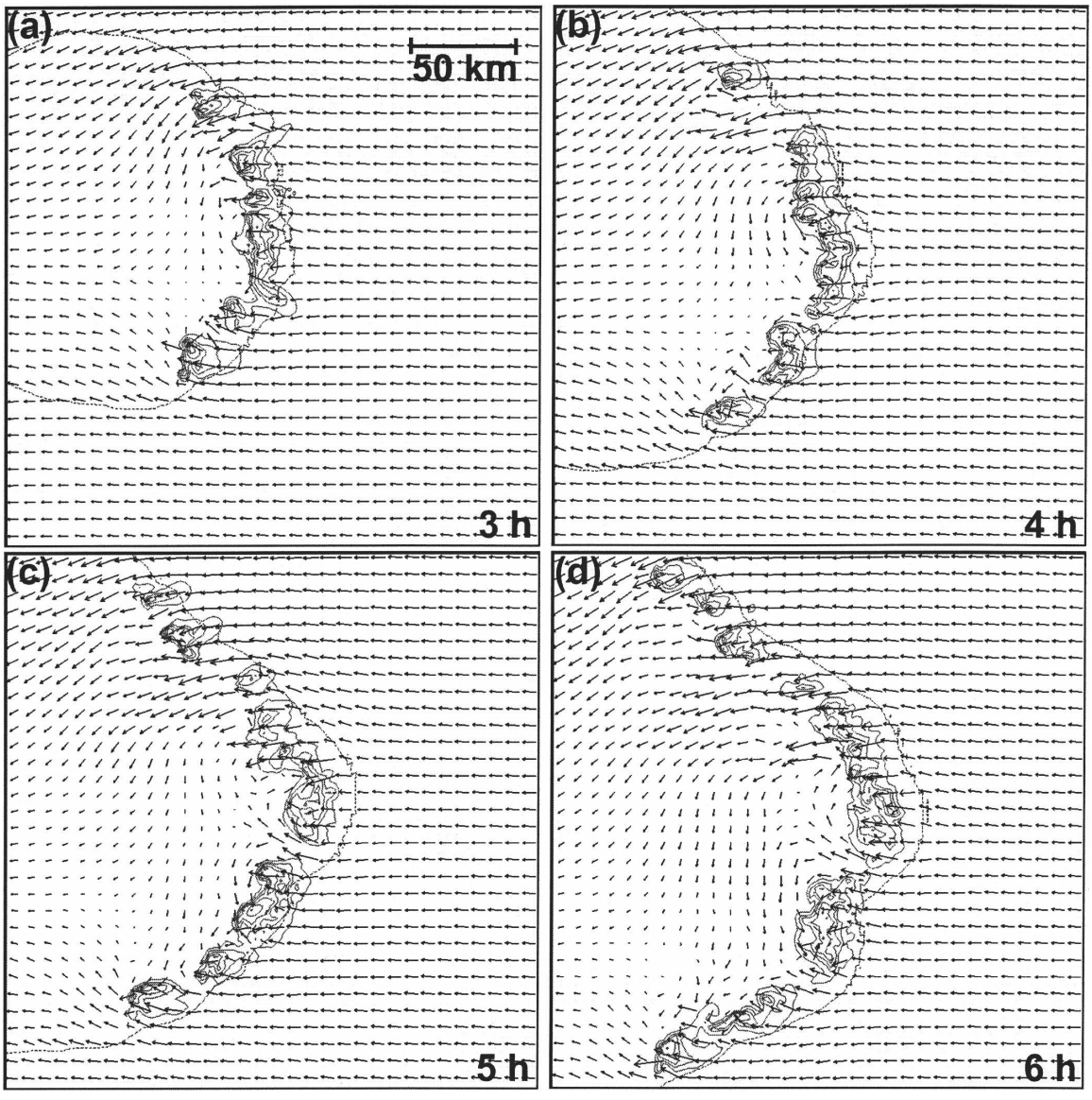

FIG. 14. As in Fig. 13 but for 3D15.

The differing behavior of the simulations is now examined closer through an inspection of the center portion of the MCSs (Fig. 16) to demonstrate further the differences in the strength and structure of the systems. The individual cells present at 2 h for 3D0 evolve quickly into a solid line of heavy precipitation about 70 km in length (Figs. 16a and 16b, left panels). As a result of this concentration of hydrometeors, the cold pool becomes very deep and responds by accelerating to a mean speed of 23–25 m s^{-1} (Fig. 17). A significant weakening of the heavy surface precipitation follows and the precipitation becomes located farther behind the gust front (Figs. 16b–d, left panels). The aerial coverage of the strong surface winds is greatest for 3D0 at this time, which is a consequence of a broad rear inflow reaching the surface as the system becomes highly tilted. For 3D15, the existence of deep shear leads to the persistence of the individual cells with more gaps in the heavy precipitation at 2.5 h (Fig. 16b, right panel). The cool pool becomes 3–4 m s^{-1} slower than for 3D0 (Fig. 17) because of a shallower cold pool, which is likely a result of the lessened concentration of hydrometeors (but may also result initially from the dynamic effects of increased upper-level shear discussed earlier in the 2D results). Concurrently, the surface precipitation remains strong and close to the gust front through 4 h for 3D15 accompanied by the eventual solidification of the heavy precipitation along the center portion of

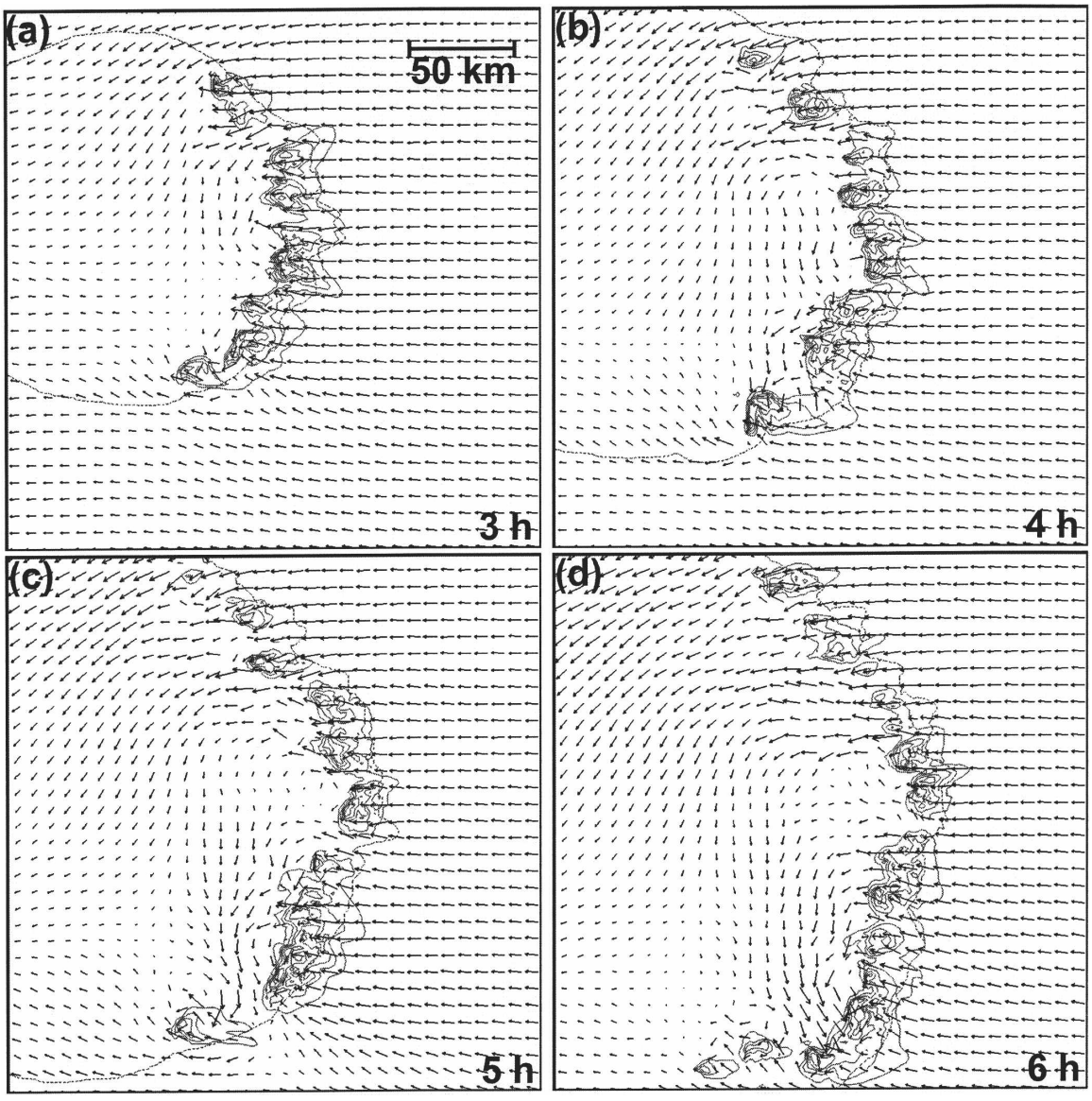

FIG. 15. As in Fig. 13 but for 3D30.

the line (Figs. 16c–e, right panels). Between 3 and 4 h, the center of the cold pool for 3D0 is broader and is accompanied with a significant weakening in the precipitation as the system becomes influenced by the broad descending rear inflow.

Storm-relative wind profiles taken ahead of the systems (Fig. 18) show that the inflow is rearward at all levels during the time that the updrafts and the surface precipitation weaken for 3D0. In this scenario all of the parcels for 3D0 have gained an increase in storm-relative rearward velocity through a faster gust front motion, but also gain rearward velocity owing to the hydrostatic lowering of pressure underneath the updraft plumes and the stronger rearward low-level buoyancy pressure accelerations related to a stronger cold pool, as discussed in PJ04. For 3D15, however, because of the existence of the upper-level shear and the somewhat slower gust front motions, the storm-relative wind profile still contains a steering level near 6.5 km (Fig. 18). The overturning persists because the midlevel front-to-rear accelerations caused by the negative buoyancy pressure perturbations in the buoyant updraft plumes are not large enough to eliminate the mean steering level that was found initially in the inflowing air.

It is interesting that the presence of more 3D struc-

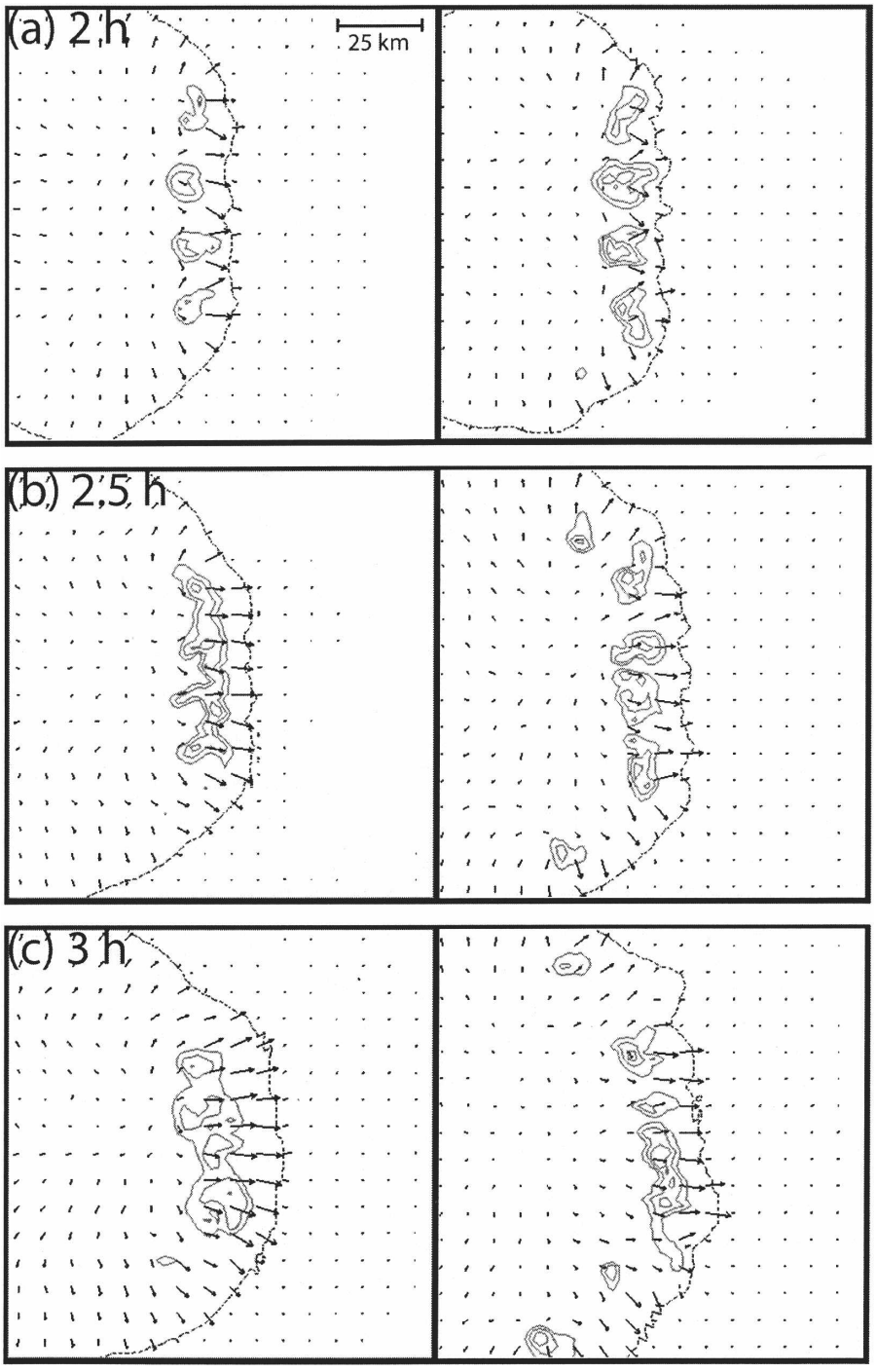

FIG. 16. A 120 km by 120 km portion of the domain with the surface total precipitation mixing ratio (solid lines every 2 g kg^{-1} starting at 2 g kg^{-1}) that highlights the heaviest precipitation, the position of the gust front at the surface (dashed line), and the ground-relative wind vectors at the surface (every four grid points) at (a) 2, (b) 2.5, (c) 3, (d) 3.5, and (e) 4 h for the case with (left) no upper-level shear (3D0) and (right) 15 m s^{-1} of upper-level shear (3D15).

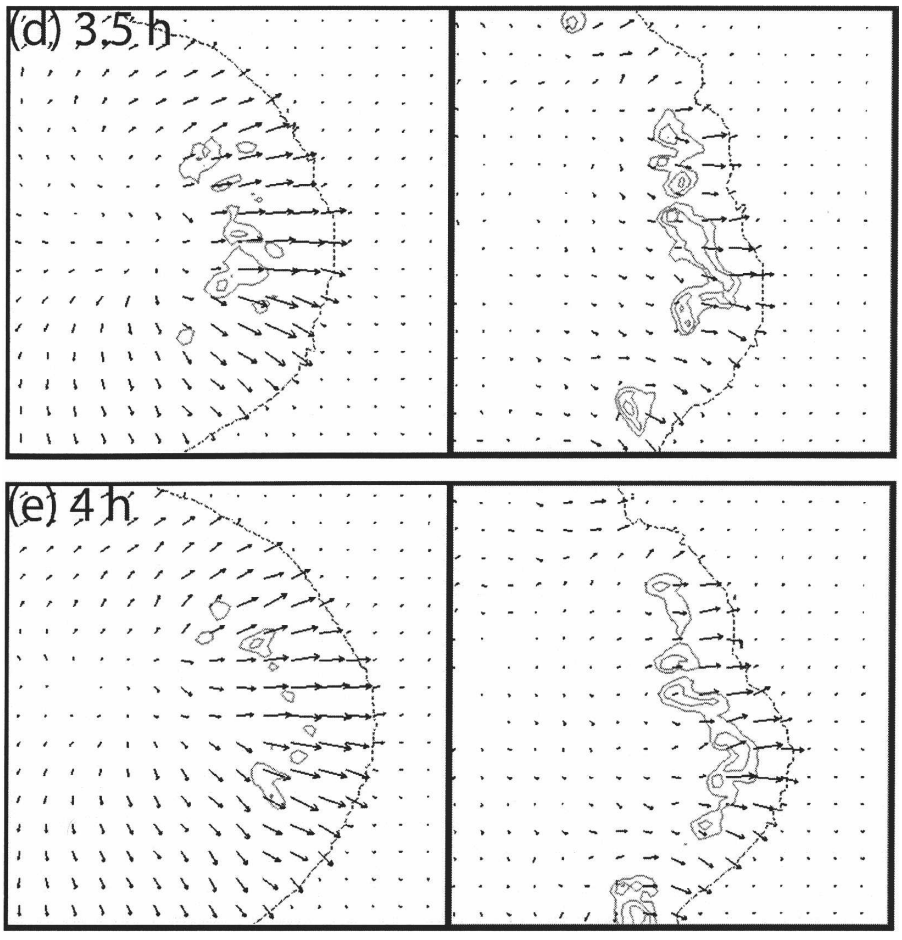

FIG. 16. (*Continued*)

tures to the cells from 2 to 3 h for 3D15 translates into a shallower cold pool and slower gust front, which reinforces the steering level in midlevels. In this sense, the upper-level shear provides a feedback to the maintenance of the steering level through the facilitation of 3D structures (Weisman et al. 1988; WR04) and the production of a shallower cold pool/slower gust front as compared to 3D0. As long as the upper-level shear is not so strong that the line will be composed entirely of supercells, this provides evidence that the effects of the upper-level shear and the maintenance of a steering level in midlevels on the behavior of the lifting can be significant even in 3D, which is highlighted next.

c. Parcel analyses

To quantify the enhancement in lifting in the 3D simulations, we calculate a series of 1-h forward-in-time trajectories beginning in the undisturbed flow at 3 h 20 min. The x and y locations for the trajectory origins trace a line that follows the contour of an 80-km portion of the gust front. Separate trajectories are calculated for each of the first ten vertical levels of the model (z = 125, 375, 625, 875, 1125, 1383, 1657, 1949, 2260, and 2591 m), which gives a total of 400 trajectory calculations for each model run. The maximum vertical displacements (δ_{max}) among the 10 vertically stacked parcels at each horizontal location are then calculated.

Results for the zero to moderate upper-level shear cases are very consistent with the behavior of the air parcels for the 2D model. Animations of the trajectories reveal that the vast majority of all of the parcels for 3D0 and most of the low-level ($z < 1$ km) parcels for 3D15 are swept rearward, while most of the elevated parcels for 3D15 are part of an overturning updraft with the upward branch located close to the leading edge of the gust front. As also found for the 2D results, the majority of the parcels responsible for this enhancement and maintenance of the deep lifting are the elevated parcels that compose an overturning updraft (Fig. 20b). The median values of the distribution in δ_{max} for the 3D results peak at a larger value of upper level shear (15 m s^{-1}) (Fig. 19) than for the 2D results (Fig.

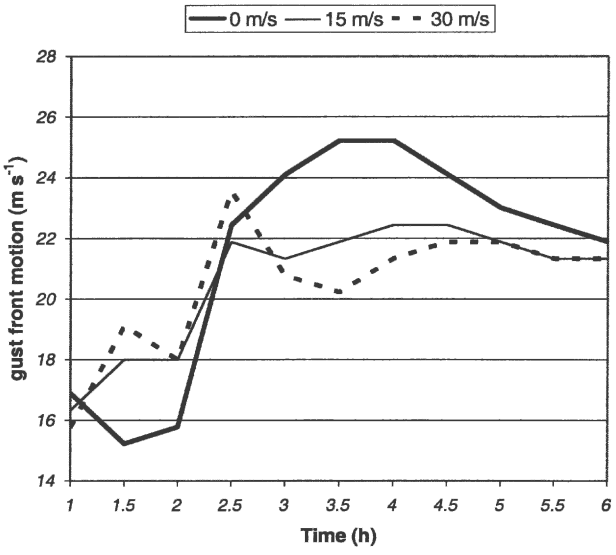

FIG. 17. Evolution of the mean half-hour gust front speed along the 100-km center portion of the gust front for the three simulations.

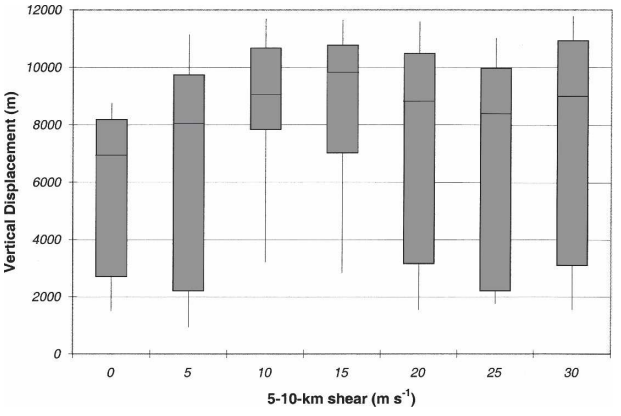

FIG. 19. Distributions of the maximum vertical parcel displacements for various values of 5–10-km shear along an 80-km portion of the line (see text for details). The lines extend to the 10th and 90th percentiles and the boxes enclose the interquartile range (25th and 75th percentiles). The thin lines within each box represent the median.

7). But the compactness of the interquartile range (25th–75th percentiles of the distribution) for δ_{max} for shear values of 10–15 m s^{-1} (Fig. 19) hints that quasi-2D deep lifting provided by the overturning is still occurring in 3D in this range of upper-level shears. As implied by Figs. 13–15, the tendency for more isolated cells to prevail and the quasi-2D lifting to be suppressed for stronger shears is evident in the stretching of the interquartile range to lower values of δ_{max} for upper-level shear values $\geq$20 m s^{-1}. But the tendency for strong, more isolated cells to persist along the line also is revealed in the persistence of some large values of δ_{max} (Fig. 19). This highlights that the reduction in 2D lifting for stronger upper-level shears shown in Fig. 7 does not directly apply to the 3D results and confirms that the stronger upper-level shears can be beneficial through the 3D processes of maintaining stronger more isolated cells and their effects on the motion of the gust front.

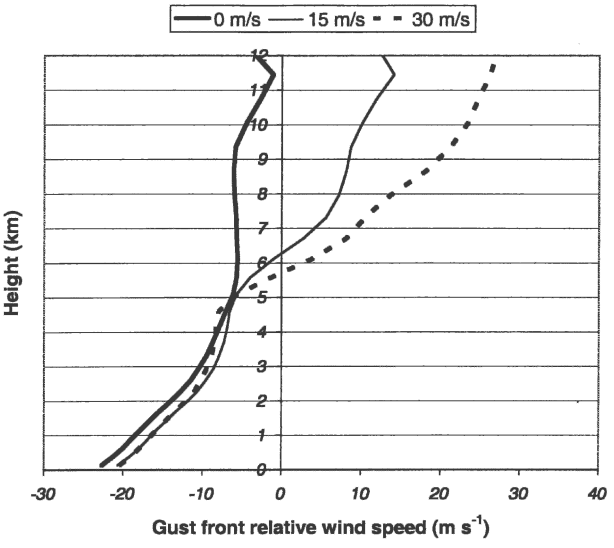

FIG. 18. The gust-front-relative ambient wind profiles for the 3D simulations at 3.5 h. To create the profiles, the u wind component is averaged in an $x = 20$ km by $y = 80$ km box centered 20 km ahead of the center portion of the gust front.

Interpretation of the distributions of δ_{max} for the 0 and 5 m s^{-1} upper-level shear cases is not as clear. But inspection of the trajectories shows that the abundance of relatively small vertical displacements, as revealed by the interquartile range of δ_{max} stretching to displacements less than 3000 m (Fig. 19), results from the tendency of the parcels that begin below 375 m to quickly become negatively buoyant as they encounter the cold pool, as found in Knupp (1987) and in Fig. 8 of PJ04a. By viewing the distribution of δ_{max} for each of the ten starting heights for 3D0 (Fig. 20a), it is evident that the bulk of the parcels that contribute to deep convective updrafts and to the broad, ascending front-to-rear flow begin at and above $z = 875$ m.

A different picture emerges for 3D15 (Fig. 20b). The distribution of δ_{max} for the parcels that begin at and below $z = 875$ m stretches toward larger displacements, even though the median values stay relatively small (Fig. 20b). This shows that more of the low-level ($z < 1$ km) parcels are lifted deeply and presumably hints that the reduction in the upshear buoyancy accelerations caused by the weaker cold pool for 3D15 help to in-

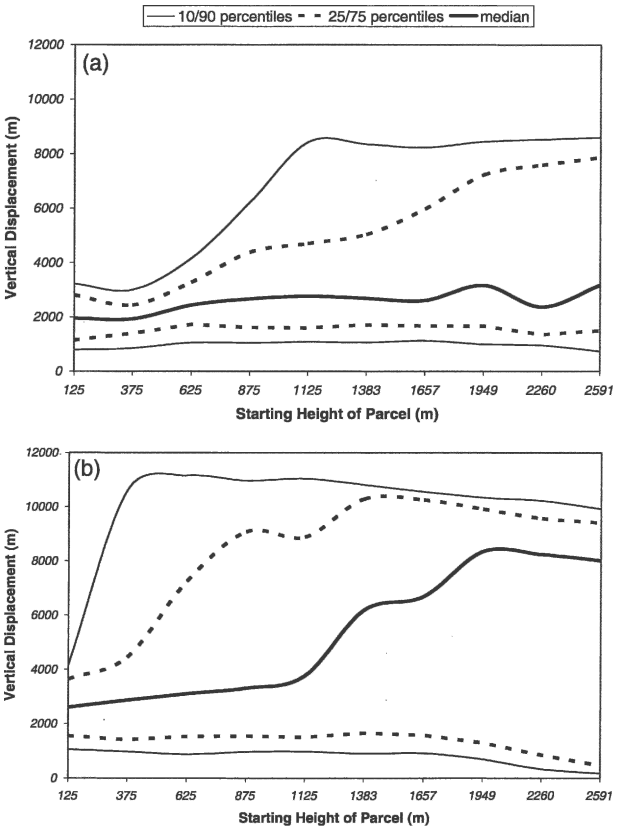

FIG. 20. Distributions of the 40 calculated maximum vertical parcel displacements along an 80-km portion of the line for each of the ten starting parcel heights (see text for details) for (a) 3D0 and (b) 3D15. The thin solid lines represent the 10th and 90th percentiles, the dashed lines represent the interquartile range (25th and 75th percentiles) and the thick solid line represents the median.

crease the likelihood that the low-level parcels convect, as discussed in PJ04 and theorized by Rotunno et al. (1988) and WR04.

However, the primary differences between the distributions of δ_{max} for 3D0 and 3D15 are seen for the elevated parcels ($z \geq 1125$ m), for which the majority are lifted to much higher levels than for 3D0 (cf. Figs. 20a,b). Additional trajectories (not shown) confirm the consistency of this overturning along the entire stretch of the cold pool and suggest that this process is largely responsible for both the maintenance of the convective updrafts along the center of the line and also for the convective triggering and maintenance along the outer flanks of the cold pool (Figs. 14 and 15). This suggests that the abundance of the deep overturning of the elevated parcels for the weak to moderate upper-level shear cases helps build on the hypotheses of S92, Moncrieff and Liu (1999), and PJ04 that the presence of this quasi-2D overturning in deep shear is an important part of the maintenance of convective lines, even when 3D structures develop.

d. Connection to observations

Subjective interpolation of the simulated MCS structures suggests that an environment with somewhere between 15 and 20 m s^{-1} of upper-level shear supports a transition from the predominance of quasi-2D structures along the arc of the cold pool and trailing stratiform precipitation to systems with significant leading stratiform precipitation (as in PJ04) and the predominance of isolated cells, although line segments and/or individual bow echoes are still found for the stronger shears (Fig. 15). We stress, however, that strong line segments and bow echoes prevail within weak to moderate upper-level shear, especially for the 10 m s^{-1} (not shown) and 15 m s^{-1} cases, with fewer gaps in the cells and less meridional flow compared to the stronger shear cases. This is different than what has been reported in the context of idealized numerical simulations within deep shear environments (Weisman et al. 1988; WR04). We also emphasize that much of the observed values of upper-level shear ahead of strong MCSs that usually contain strong line segments and bow echoes (Pryzbylinski 1995; Miller and Johns 2000; C04) are found in this very range (5–20 m s^{-1}) (C04).

With this in mind, it is enlightening to briefly return to observations of shear profiles taken ahead of strong midlatitude MCSs. Mean storm-relative hodographs from soundings[3] that sample the mature and decay environments show that significant unidirectional upper-level shear with a mean steering level near 8 km is present as MCSs mature (Fig. 21), which is often tied to preexisting upper-level jets (C04). However, this upper-level shear decreases significantly and the steering level disappears as the MCSs decay (Fig. 21). This decrease in upper-level shear can often be traced to the propagation of the MCS away from the upper-level jet. Because of the decrease in upper-level shear, rearward storm-relative flow $\geq$6 m s^{-1} is found at all levels for the decay soundings (Fig. 21). This wind profile is similar to what is found in the simulated environment for 3D0 (Fig. 18) as the updrafts and precipitation weaken and the system becomes highly slanted. In the context of this study, the important point from Fig. 21 is that the

[3] Note that soundings that are taken within strongly forced synoptic-scale environments are not included in Fig. 21 (Fig. 14 of C04 does include these soundings). Therefore, the updated hodographs shown in Fig. 21 are more representative of the type of MCSs that are being studied here than the hodographs shown in C04.

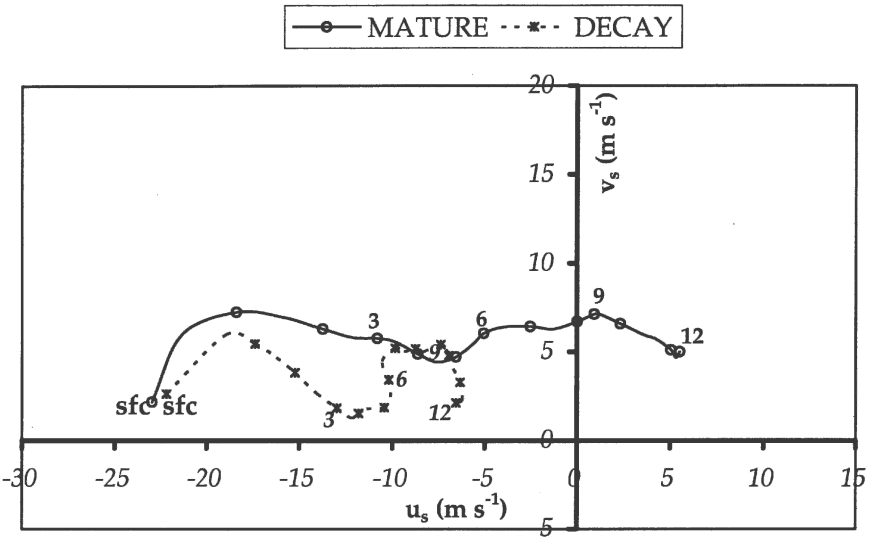

FIG. 21. Mean storm-relative hodographs for a set of 79 proximity soundings taken in the environment of strong warm-season midlatitude MCSs grouped into 35 soundings that sampled the environment ahead of mature MCSs and 44 soundings that sampled the environment ahead of decaying MCSs. The hodographs are calculated with the mean winds at every 0.5 km AGL. The mean winds are plotted every 1 km AGL and labeled every 3 km AGL. The abscissa is aligned with the MCS motion vector prior to averaging to preserve the relative flow vectors. The steering level is found where the hodograph for the mature MCSs crosses the v_s axis.

disappearance of the steering level in the observations is primarily due to the reduction of upper-level shear in the environment. Although the low-level shear and storm-relative inflow decrease somewhat toward decay, which may be contributing to the MCS decay to some degree, the significant weakening of the upper-level shear and the disappearance of the steering level provides observational evidence that the overturning process is a significant component to the complex question of MCS structure and maintenance in many cases.

5. Summary and final discussion

The goal of this study is to build on recent numerical modeling studies that examine the role of upper-level wind shear on the evolution of strong midlatitude MCSs. We are motivated by observations from past research that deep shear is common to these MCS environments, yet these environments have not been emphasized in past modeling studies. The dependence of lifting of environmental air above a cold pool on the upper-level wind shear is first quantified with idealized 2D simulations. The effects of upper-level shear on the structure and maintenance of MCSs under more realistic conditions are examined with 3D simulations.

For cold pools in a 2D environment with 20 m s^{-1} of shear in the lowest 5 km, it is found that the addition of weak to moderate shear in the 5–10-km layer allows for the development of an overturning circulation that lifts parcels from the 1–2-km layer to higher levels than any parcels without upper-level shear in the environment. The deeper lifting, which is maximized for 5- to 10-km shear values somewhere between 5 and 10 m s^{-1}, occurs despite a reduction of vertical velocity resulting from the decrease in the head depth of the cold pool. In the environments with upper-level shear, the overturning parcels remain close to the leading edge of the gust front during their rapid ascent, whereas all of the parcels in the low-level inflow for the no upper-level shear case are swept rearward as they are forced over the cold pool. This is a consequence of weak storm-relative flow (a steering level) being maintained in midlevels, which is facilitated by deep shear environments. As the upper-level shear becomes stronger (>0 m s^{-1}) in the 2D simulations, the high perturbation pressure aloft that is a dynamic response to the stagnation point in the flow reduces the vertical scale of the overturning and begins a decreasing trend in the vertical displacement of the overturning parcels.

A main result from the 3D simulations is that the overturning process that results from the upper-level shear maintains strong and more upright updrafts close to the gust front. Calculations of the vertical displacement of parcels among the 3D simulations confirm that

the overturning of elevated parcels is largely responsible for the deeper lifting, which is maximized for upper-level shears between 10 and 15 m s^{-1} and, consequently, the development and maintenance of the convection. The detriment of stronger upper-level shear on the lifting found for the 2D results is manifest in the 3D results as a transition from quasi-linear systems with strong line segments and bow echoes for upper-level shears of 5–15 m s^{-1} to systems with predominantly leading stratiform precipitation and the prevalence of more isolated 3D structures for upper-level shears $\geq$20 m s^{-1}, although line segments and bow echoes can still occur under the stronger upper-level shears. An additional effect of the overturning in 3D for all nonzero upper-level shears is to greatly increase the size of the MCS through the combination of the slower cold pool and the overturning that increases the likelihood of convective initiation along the flanks of the cold pool. The upper-level shear provides a potential feedback to the overturning process by facilitating more isolated convective cells initially, which results in a shallower cold pool and slower gust front than for the no upper-level shear case. This slower gust front helps to maintain the steering level in midlevels, which encourages the continued horizontal placement of the updrafts close to the gust front.

The fact that the enhancement in lifting provided by upper-level shear occurs for the elevated parcels may help explain how strong MCSs are maintained, even without the benefits provided by a low-level jet (Augustine and Caracena 1994; Arritt et al. 1997; Fritsch and Forbes 2001). If the surface nocturnal inversion does not prevent the replenishment of a deep cold pool, the lifting and overturning of the elevated high-θ_e air can continue well after dark. The synthesis of PJ04a provides a summary of observations of these types of systems in which this process may have occurred. Furthermore, we encourage the reader to inspect the vertical cross sections and environmental soundings obtained from the 9–10 June 2003 nocturnal bow echo–MCS event during the Bow Echoes and Mesoscale Convective Vortex (BAMEX) field experiment (see Fig. 6 in Davis et al. 2004). The observed flow structure obtained with high-quality multiple Doppler radar analysis strongly suggests that the parcels originating above 2 km are overturning deeply and the parcels below this level are passing through the cold pool region (see their Fig. 6). The shear profile above the inversion is complex, but includes layers of significant shear above 3 km, which suggests that the elevated overturning process described in PJ04 and herein was important for this event (see their Fig. 6).

Lastly, we do not to intend to discount the importance of the low-level shear. Indeed, past research shows that low-level shear is usually observed in the environment and is needed to simulate long-lived convective systems (Thorpe et al. 1982; Rotunno et al. 1988; C04). It is also recognized that the overall strength and structure of simulated MCSs is clearly sensitive to the low-level shear and the systems tend to be stronger with larger values of low-level shear (PJ04a; WR04). Although we do not know the relative sensitivities between the addition of shear in low levels versus upper levels, we have shown that upper-level shear, added to an environment with low-level shear, can have a significant impact on the structure and evolution of the simulated systems and have provided a link to the presence of strong, deep shear that is typically observed in the environments of strong quasi-linear midlatitude MCSs. Indeed, the results (Figs. 19 and 21 especially) point to a straightforward application to forecasting the structure and longevity of strong MCSs given a forecast of the cold pool motion and the environmental shear profile. Since the motion of the cold pool is very difficult to forecast prior to convective initiation (Corfidi 2003), the most suitable application of the overturning concept may be the prediction of the demise of an MCS after a cold pool motion can be gauged accurately, although recent efforts to use the deep shear profile to forecast the maintenance of strong MCSs without knowledge of the cold pool motion are promising (see Coniglio et al. 2005).

Acknowledgments. We are grateful to Drs. Alan Shapiro and Qin Xu for the insightful discussions and for providing the impetus for this study. We thank Dr. Matt Parker for his openness and his very constructive review of this manuscript. The manuscript was also improved significantly by the comments provided by an anonymous reviewer. Drs. Lance Bosart and Robert Fovell provided very helpful comments to this study. We also value the continuing discussions with Dr. Morris Weisman. We thank Victor Homar for his help in generating some of the figures for this work. Funding for this work was provided by NSF Grant ATM0244846 through a cooperative agreement between the National Oceanic and Atmospheric Administration and the University of Oklahoma.

APPENDIX

Description of the NCOMMAS Model

The NSSL Collaborative Model for multiscale atmospheric simulation was first developed in the early 1990s by the third author to be used to study the dy-

namics of supercell and tornado genesis. Over the past seven years the model has changed considerably, and this appendix documents the current equation set and numerical algorithms used to integrate the model.

The equation set is that originally used by Klemp and Wilhelmson (1978, hereafter, KW78). The current model includes a prognostic equation for turbulent kinetic energy as well as a Smagorinsky mixing scheme. For the simulations presented in this paper, the Smagorinsky scheme was used. The governing equations are

$$\frac{du_i}{dt} = -C_p\bar{\theta}\frac{\partial \pi'}{\partial x_i} - \varepsilon_{ijk}f_j(u_k - \bar{u}_k) + \delta_{i3}B + D_i$$

$$B = g\left[\frac{\theta - \bar{\theta}}{\bar{\theta}} + 0.61(q_v - \bar{q}_v) + \sum_l q_l + \sum_i q_i\right]$$

$$D_i = \frac{\partial}{\partial x_i}\left[K_m\left(\frac{\partial u_i}{\partial x_j} + \frac{\partial u_j}{\partial x_i}\right) + \frac{2}{3}\delta_{ij}E\right] \tag{A1}$$

$$\frac{\partial \pi'}{\partial t} + \frac{C_s^2}{C_p\bar{\rho}\bar{\theta}_v}\frac{\partial(\bar{\rho}u_i)}{\partial x_i} = F_\pi. \tag{A2}$$

The variables use KW78 notation. Buoyancy effects from hydrometeor loading are accounted for in the summations over the liquid and ice hydrometeor mixing ratios, respectively, and the D are the turbulent mixing terms (which are identical to those described in KW78). Variables with overbars represent the vertical background states used to increase numerical accuracy. The perturbation Exner function is used for the pressure; again, the vertical background state has been subtracted from the equations. As in most cloud-scale models the F_π term is set to zero as it primarily changes the mean pressure within the domain that, like anelastic formulations, impacts the dynamical solution minimally.

The thermodynamic and hydrometeor equations are given by

$$\frac{d\theta}{dt} = D_\theta + M_\theta$$

$$D_\theta = \frac{\partial}{\partial x_i}\left(K_m\frac{\partial \theta}{\partial x_i}\right) \tag{A3}$$

$$\frac{dq_i}{dt} = -\frac{1}{\bar{\rho}}\frac{\partial(\bar{\rho}V_{T_i}q_i)}{\partial z} + D_{q_i} + M_{q_i}, \quad \text{where}$$

$$q_i = q_v, q_c, q_r, q_i, q_s, q_h$$

$$D_{q_i} = \frac{\partial}{\partial x_i}\left(K_m\frac{\partial q_i}{\partial x_i}\right). \tag{A4}$$

The first term on the right-hand size of (A4) represents the hydrometeor fallout and the M_x represent the microphysical sources and sinks. A Lin–Farley–Orville three-class ice scheme is used for the microphysical parameterization; see Gilmore et al. (2004a,b) for the details. In the Gilmore et al. scheme all liquid and ice hydrometeors have a terminal velocity, except cloud water.

The parameterization of the turbulent mixing coefficient is represented using a prognostic turbulent kinetic energy (TKE) equation to represent the energy associated with the subgrid scale eddies. Here we use a somewhat different formulation than KW78. In KW78 the mixing length was a constant and therefore could be included into the equation for TKE in a straightforward manner. The use of grid stretching and anisotropic grid spacing introduces a variable mixing length that is no longer constant. Therefore this length scale is removed from the KW78 equation for the turbulent mixing coefficient. The resulting TKE equation is similar to that used by Deardorff (1980) and written as

$$\frac{dE^{1/2}}{dt} = \frac{C_m l}{2}[\text{shear}] - \frac{P_r C_m l}{2}[\text{buoy}] + \frac{\partial}{\partial x_i}\left[2K_m\frac{\partial E^{1/2}}{\partial x_i}\right] - \frac{C_e E}{2l}, \tag{A5}$$

$$K_m = C_m l E^{1/2},$$

where the shear and buoy terms are given by Eqs. (2.19) and (2.24) in KW78, respectively. These simulations use values of $C_m = 0.21$ and $C_e = 0.7$. The length scale is computed as the cube root of the computational grid volume or as a function of distance from the lower boundary. In the Smagorinsky mixing scheme used in the research here, K_m is given via

$$K_m = (C_m l)^2\sqrt{\max(\text{shear} - P_r\,\text{buoy}, 0)}. \tag{A6}$$

The numerical integration scheme for the velocity and pressure equations closely follows that of Wicker and Skamarock (2002). A third-order Runge–Kutta time integration scheme is used with fifth-order (third order) finite difference approximations for the spatial derivatives in the horizontal (vertical). Fluxes are computed using a velocity field that is locally nondivergent for each grid zone. This nondivergent approximation is similar to other approaches (Tripoli 1992). As a numerical filter, the fluxes on the last iteration of the Runge–Kutta scheme are computed using the weighted essentially nonoscillatory (WENO) scheme as described by Shu (2001). The use of WENO finite differencing on only the last iteration reduces the cost of the scheme while retaining almost all of the desired filtering properties. Potential temperature advection also uses the WENO approximation on the last Runge–

Kutta integrations. For TKE and hydrometeor transport, the same time and spatial integration scheme is used for momentum except on the last iteration; Thuburn's (1995) one-dimensional monotonic limiter is applied along each coordinate direction. While separate one-dimensional application of the limiter does not guarantee positive definite fluxes for three-dimensional advection, it sufficiently removes undershoots such that only small amounts of numerical hole filling are needed to ensure positivity. The use of the Thurburn limiter only on the last iteration again reduces the cost of the scheme, while retaining the desired filtering effects. Vertical fluxes from hydrometeor fallout are computed using a first-order upwind method.

The mixing and pressure gradient terms are approximated with second-order finite differences. Mixing terms are computed only once via a forward-in-time method. The divergence pressure gradients are computed using the standard forward–backward scheme on the staggered C grid. Rayleigh damping is applied to the fields near the top of the domain. Other than the Rayleigh damping and the WENO and Thuburn filters for the advective fluxes, no other filtering is used during the model integration.

REFERENCES

Arritt, T. R., M. Segal, D. P. Todey, C. A. Clark, M. J. Mitchell, and K. M. Labas, 1997: The Great Plains low-level jet during the warm season of 1993. *Mon. Wea. Rev.,* **125,** 2176–2192.

Augustine, J. A., and F. Caracena, 1994: Lower-tropospheric precursors to nocturnal MCS development over the central United States. *Wea. Forecasting,* **9,** 116–135.

Bryan, G. H., J. C. Wyngaard, and J. M. Fritsch, 2003: Resolution requirements for the simulation of deep moist convection. *Mon. Wea. Rev.,* **131,** 2394–2416.

Burke, P. C., and D. M. Schultz, 2004: A 4-yr climatology of cold-season bow echoes over the continental United States. *Wea. Forecasting,* **19,** 1061–1074.

Coniglio, M. C., and D. J. Stensrud, 2001: Simulation of a progressive derecho using composite initial conditions. *Mon. Wea. Rev.,* **129,** 1593–1616.

——, ——, and M. B. Richman, 2004: An observational study of derecho-producing convective systems. *Wea. Forecasting,* **19,** 320–337.

——, H. E. Brooks, and S. J. Weiss, 2005: Use of proximity sounding parameters to improve the prediction of MCS speed and demise. Preprints, *21st Conf. on Weather Analysis and Forecasting,* Washington, DC, Amer. Meteor. Soc., 3.3.

Corfidi, S. F., 2003: Cold pools and MCS propagation: Forecasting the motion of downwind-developing MCSs. *Wea. Forecasting,* **18,** 997–1017.

Davis, C. A., and Coauthors, 2004: The Bow-Echo and MCV Experiment (BAMEX): Observations and opportunities. *Bull. Amer. Meteor. Soc.,* **85,** 1075–1093.

Deardorff, J. W., 1980: Stratocumulus-capped mixed layers derived from a three-dimensional model. *Bound.-Layer Meteor.,* **18,** 495–527.

Droegemeier, K. K., and R. B. Wilhelmson, 1987: Numerical simulation of thunderstorm outflow dynamics. Part I: Outflow sensitivity experiments and turbulence dynamics. *J. Atmos. Sci.,* **44,** 1180–1210.

Fritsch, J. M., and G. S. Forbes, 2001: Mesoscale convective systems. *Severe Convective Storms, Meteor. Monogr.,* No. 38, C. Doswell III, Ed., Amer. Meteor. Soc., 323–357.

——, R. J. Kane, and C. R. Chelius, 1986: The contribution of mesoscale convective weather systems to the warm season precipitation in the United States. *J. Climate Appl. Meteor.,* **25,** 1333–1345.

Gale, J. J., W. A. Gallus Jr., and K. A. Jungbluth, 2002: Toward improved prediction of mesoscale convective system dissipation. *Wea. Forecasting,* **17,** 856–872.

Gilmore, M. S., J. M. Straka, and E. N. Rasmussen, 2004a: Precipitation and evolution sensitivity in simulated deep convective storms: Comparisons between liquid-only and simple ice and liquid phase microphysics. *Mon. Wea. Rev.,* **132,** 1897–1916.

——, ——, and ——, 2004b: Precipitation uncertainty due to variations in precipitation particle parameters within a simple microphysics scheme. *Mon. Wea. Rev.,* **132,** 2610–2627.

Houze, R. A., Jr., S. A. Rutledge, M. I. Biggerstaff, and B. F. Smull, 1989: Interpretation of Doppler weather radar displays of midlatitude mesoscale convective systems. *Bull. Amer. Meteor. Soc.,* **70,** 608–619.

Johns, R. H., and W. D. Hirt, 1987: Derechos: Widespread convectively induced windstorms. *Wea. Forecasting,* **2,** 32–49.

Klemp, J. B., and R. B. Wilhelmson, 1978: The simulation of three-dimensional convective storm dynamics. *J. Atmos. Sci.,* **35,** 1070–1096.

Knupp, K. R., 1987: Downdrafts within high plains cumulonimbi. Part I: General kinematic structure. *J. Atmos. Sci.,* **44,** 987–1008.

Laing, A. G., and J. M. Fritsch, 2000: The large-scale environments of the global populations of mesoscale convective complexes. *Mon. Wea. Rev.,* **128,** 2756–2776.

LeMone, M. A., E. J. Zipser, and S. B. Trier, 1998: The role of environmental shear and thermodynamic conditions in determining the structure and evolution of mesoscale convective systems during TOGA COARE. *J. Atmos. Sci.,* **55,** 3493–3518.

Lin, Y., R. D. Farley, and H. D. Orville, 1983: Bulk parameterization of the snow field in a cloud model. *J. Climate Appl. Meteor.,* **22,** 1065–1092.

Liu, C., and M. W. Moncrieff, 1996: A numerical study of the effects of ambient flow and shear on density currents. *Mon. Wea. Rev.,* **124,** 2282–2303.

Miller, D. J., and R. H. Johns, 2000: A detailed look at extreme wind damage in derecho events. Preprints, *20th Conf. on Severe Local Storms,* Orlando, FL, Amer. Meteor. Soc., 52–55.

Moncrieff, M. W., 1992: Organized convective systems: Archetypal dynamical models, mass and momentum flux theory, and parameterization. *Quart. J. Roy. Meteor. Soc.,* **118,** 819–850.

——, and C. Liu, 1999: Convection initiation by density currents: Role of convergence, shear, and dynamical organization. *Mon. Wea. Rev.,* **127,** 2455–2464.

Parker, M. D., and R. H. Johnson, 2000: Organizational modes of midlatitude mesoscale convective systems. *Mon. Wea. Rev.,* **128,** 3413–3436.

——, and ——, 2004a: Structures and dynamics of quasi-2D mesoscale convective systems. *J. Atmos. Sci.,* **61,** 545–567.

——, and ——, 2004b: Simulated convective lines with leading precipitation. Part I: Governing dynamics. *J. Atmos. Sci.,* **61,** 1637–1655.

——, and ——, 2004c: Simulated convective lines with leading precipitation. Part II: Evolution and maintenance. *J. Atmos. Sci.,* **61,** 1656–1673.

Pryzbylinski, R. W., 1995: The bow echo: Observations, numerical simulations, and severe weather detection methods. *Wea. Forecasting,* **10,** 203–218.

Rotunno, R., J. B. Klemp, and M. L. Weisman, 1988: A theory for strong, long-lived squall lines. *J. Atmos. Sci.,* **45,** 463–485.

Seitter, K. L., 1986: A numerical study of atmospheric density current motion including the effects of condensation. *J. Atmos. Sci.,* **43,** 3068–3076.

Shapiro, A., 1992: A hydrodynamical model of shear flow over semi-infinite barriers with application to density currents. *J. Atmos. Sci.,* **49,** 2293–2305.

Shu, C.-W., 2001: High order finite difference and finite volume WENO schemes and discontinuous Galerkin methods for CFD. ICASE Rep. 2001-11, NASA/CR-2001-210865, 17 pp. [Available from ICASE, NASA Langley Research Center, M. S. 132C, 3 West Reid St., Building 1152, Hampton, VA 23681-2199; available online at http://www.icase.edu.]

Staniforth, A., and J. Côté, 1991: Semi-Lagrangian integration schemes for atmospheric models—A review. *Mon. Wea. Rev.,* **119,** 2206–2223.

Stensrud, D. J., M. C. Coniglio, R. Davies-Jones, and J. Evans, 2005: Comments on "A theory for strong long-lived squall lines' revisited." *J. Atmos. Sci.,* **62,** 2989–2996.

Thorpe, A. J., M. J. Miller, and M. W. Moncrieff, 1982: Two-dimensional convection in non-constant shear: A model of mid-latitude squall lines. *Quart. J. Roy. Meteor. Soc.,* **108,** 739–760.

Thuburn, J., 1995: Dissipation and cascades to small scales in numerical models using a shape-preserving advection scheme. *Mon. Wea. Rev.,* **123,** 1888–1903.

Tripoli, G. J., 1992: A nonhydrostatic mesoscale model designed to simulate scale interaction. *Mon. Wea. Rev.,* **120,** 1342–1359.

Weisman, M. L., and J. B. Klemp, 1982: The dependence of numerically simulated convective storms on vertical wind shear and buoyancy. *Mon. Wea. Rev.,* **110,** 504–520.

——, and R. J. Trapp, 2003: Low-level mesovortices within squall lines and bow echoes. Part I: Overview and dependence on environmental shear. *Mon. Wea. Rev.,* **131,** 2779–2803.

——, and R. Rotunno, 2004: "A theory for strong, long-lived squall lines" revisted. *J. Atmos. Sci.,* **61,** 361–382.

——, J. B. Klemp, and R. Rotunno, 1988: Structure and evolution of numerically simulated squall lines. *J. Atmos. Sci.,* **45,** 1990–2013.

——, W. C. Skamarock, and J. B. Klemp, 1997: The resolution dependence of explicitly modeled convective systems. *Mon. Wea. Rev.,* **125,** 527–548.

Wicker, L. J., and W. C. Skamarock, 2002: Time-splitting methods for elastic models using forward time schemes. *Mon. Wea. Rev.,* **130,** 2088–2097.

Xu, Q., 1992: Density currents in shear flows—A two-fluid model. *J. Atmos. Sci.,* **49,** 511–524.

——, and M. W. Moncrieff, 1994: Density current circulations in shear flows. *J. Atmos. Sci.,* **51,** 434–446.

Xue, M., 2000: Density currents in two-layer shear flows. *Quart. J. Roy. Meteor. Sci.,* **126,** 1301–1320.

——, Q. Xu, and K. K. Droegemeier, 1997: A theoretical and numerical study of density currents in nonconstant shear flows. *J. Atmos. Sci.,* **54,** 1998–2019.

Zipser, E. J., 1982: Use of a conceptual model of the life cycle of mesoscale convective systems to improve very-short-range forecasts. *Nowcasting,* K. Browning, Ed., Academic Press, 191–221.